Prediction of bias-voltage-dependent corrugation reversal for STM images of bcc (110) surfaces: W(110), Ta(110), and Fe(110)

S. Heinze
Institut für Festkörperforschung, Forschungszentrum Jülich, D-52425 Jülich, Germany
and Zentrum für Mikrostrukturforschung, Universität Hamburg, D-20355 Hamburg, Germany

S. Blügel*
Institut für Festkörperforschung, Forschungszentrum Jülich, D-52425 Jülich, Germany

R. Pascal, M. Bode, and R. Wiesendanger
Zentrum für Mikrostrukturforschung, Universität Hamburg, D-20355 Hamburg, Germany
(Received 15 July 1998)

We predict a bias-voltage dependent corrugation reversal for scanning tunneling microscopy (STM) images with atomic resolution of bcc-(110) transition metal surfaces: Atoms which appear usually on STM images of metal surfaces as protrusions, may appear on these images anticorrugated, e.g., as hollow sites and *vice versa* hollow sites may appear as atoms. This makes the absolute determination of atom sites by STM unreliable. We investigate the image-reversal in detail for the W(110) surface and explain its origin on the basis of the electronic structure. We found, the image is determined by a competition between surface resonance states with d_{xz} and d_{z^2} character contributing to a direct image of atomic sites and surface-state bands around the $\overline{S}$ point of the two-dimensional Brillouin zone with pd bonding character and bonding charge between the surface atoms. The surface states contribute to anticorrugated images. Finally the image depends on the bias voltage. For W(110) and positive bias voltages the surface resonances dominate over the surface states leading to a direct image of atomic sites. For negative voltages below a critical value of -0.4 V calculations show a reversed image, i.e., anticorrugation. The critical bias voltage depends slightly on the tip-sample separation. For bias voltages around the critical value corrugating and anticorrugating contributions to the STM image compensate each other, the corrugation amplitudes become extremely small, the atomic resolution disappears, which is consistent with the experimental difficulties in achieving atomic resolution on W(110) for negative voltages and stripelike images are predicted. For positive bias voltages we found a good agreement between the theoretical results and our measured STM images. The competition between surface resonances and surface states is a quite general mechanism and anticorrugation is expected to occur on (110) surfaces of other bcc transition-metals [i.e., Nb(110), Mo(110), Ta(110)]. We demonstrated this explicitly for Ta(110), anticorrugation occurs practically over the entire bias-voltage range available by a STM and an image reversal from an anticorrugated to a corrugated image is predicted for 1.3 V. For magnetic surfaces the image reversal may occur twice, once for majority and once for minority states. For Fe(110) we show that the minority spin channel controls the STM image. We predict a direct image for majority states and an anticorrugated image for minority states below a bias voltage of 0.7 V, and we predict only one image reversal at about 0.4 V for an ordinary non-spin-polarized STM. Employing the full-potential linearized augmented plane wave method in film geometry, the electronic structure is determined by first principles calculations within the framework of the density functional theory in the local (spin) density approximation. The STM analysis is carried out within the *s*-orbital tip-model of Tersoff and Hamann. An efficient analysis of the corrugation amplitude in terms of two-dimensional star coefficients of the vacuum density of states is presented. The tip-sample distance dependent $\mathbf{k}_{\|}$-point selection to the tunneling current is analyzed. The enhancement of the corrugation amplitude due to p_z- and d_{z^2}-type tip-orbitals are determined. We show that the enhancement factors calculated are close to the analytical factors given by Chen. [S0163-1829(98)04347-1]

I. INTRODUCTION

The scanning tunneling microscope (STM) developed to a very powerful real-space probe to image the surface topography. However, as the resolution of the STM has reached the atomic scale,[1] the interpretation of STM images possesses some difficulties. The key problem arises from the physical effect applied by the STM, which is the tunneling of electrons between a sample surface and a tip. This makes the separation between the geometrical and electronic structure very difficult. Often a first idea for the interpretation of the surface topography comes from the symmetries of the atomic structure reflected by the image. But this is mostly insufficient for the chemical identification of atoms at compound surfaces, defects, adsorbates or even the correct assignment of atom sites. Thus the key to the interpretation of an STM image is the knowledge of the electronic structure as has been pointed out by Tersoff and Hamann.[2]

Experience over the past ten years has proven that the knowledge of the electronic structure is particularly impor-

tant for the interpretation of topography images for surfaces of covalently bonded semiconductors,[3–8] which show spatially oriented occupied and unoccupied dangling bonds. In this case the STM image may differ drastically from a surface topography. A crucial experimental clue for the interpretation of images on the basis of the electronic structure is provided by the dependence of the image upon tunnel voltage. The combination of voltage dependent images with theoretical electronic structure calculations developed to a powerful approach for the analysis of atomically resolved images.[6–11]

On the other hand, for metals the conventional wisdom[12] says that the interpretation of metal surfaces is fairly straightforward and rather simple: In metals, electrons screen the nuclear charge and thus follow to a good approximation the atomic structure. Thus areas of high and low tunneling current should be assigned to protruding atoms or atomic interstices, respectively. The STM image may correspond quite closely to a topography of the surface, even on the atomic scale. This type of interpretation has been widely used for atomically resolved STM images of metal surfaces.[13–15]

Although this argument might be true for simple metals such as Au, Al, or Cu, in this paper we give theoretical evidence that for transition-metal surfaces the interpretation of STM images is far from being trivial. For W(110) we predict anticorrugation for negative bias voltages below a certain voltage, e.g., changing the bias voltage leads to an inversion of the corrugation: protruding atoms appear as atomic interstices and *vice versa*. This makes a reliable assignment of atom positions impossible. In the voltage regime where image reversal takes place, it is even possible that a stripelike topography appears, which results from the competition between corrugating and anticorrugating electronic states, and atomic resolution might become impossible. In particular, for W(110) we found that this transient voltage regime stretches between -0.4 V and 0 V and that the corrugation amplitude becomes extremely small. We speculate that this might be the origin of the big experimental difficulties in resolving the W(110) surface with atomic resolution at negative bias voltages.

We explain anticorrugation on the basis of the electronic structure. We show that the STM image is determined by a competition between surface resonance states with d_{xz} and d_{z^2} character contributing normal STM images with atoms appearing as protrusions and surface-state bands around the $\bar{S}$ point of the two-dimensional Brillouin zone contributing to an unusual anticorrugated image. The surface state is of pd bonding character, with a minimum energy of 1.3 eV below the Fermi energy, crossing the Fermi energy and changing from mainly d to p type. The surface states are split-off states of bonding bulk pd states with bonding charges between the atoms along the short side of the centered rectangular unit cell of the bcc (110) surface. As the surface is formed, a split-off state appears due to the change of the potential at the surface, the bond strength between atoms at the forming surface increases, the hybridization of this state with the underlying substrate decreases, the charge density of the so formed surface state releases energy by spilling out into the vacuum and causes the anticorrugation.

We have selected the W(110) surface because it is widely used for the growth of thin films and the exact position of the atoms is an important information and even essential, if one tries to decide upon adsorption sites. We think, however, that this anticorrugation is a general phenomenon at bcc (110) surfaces. We comment on the anticorrugation of Mo(110), Nb(110), and Ta(110) and with Fe(110) we discuss a second example in detail. In fact, we speculate that anticorrugation is a quite general phenomenon on transition-metal surfaces.

Anticorrugation has been discussed before in the context of transition-metal surfaces as a tip-induced effect[16] at small tip-sample separations. In contrast, the anticorrugation we discuss here is an intrinsic effect due to the electronic structure of the sample. Section II outlines shortly the theoretical determination of the STM images. Sections III and IV describe the computational and experimental details. In Sec. V we present our results and explain the effect by analyzing the calculated electronic structure. Finally, Sec. VI summarizes our results.

II. THEORETICAL MODEL

In this paper, STM images were calculated on the basis of the model of Tersoff and Hamann,[2] which has been successfully applied in connection with *ab initio* calculations of semiconductor surfaces,[6–8] transition-metal silicides,[9] and transition-metal surfaces.[10,11] In this model the transition probability or tunneling current I as a function of the bias voltage V can be expressed exclusively by sample properties:

$$
\begin{aligned}
I(\mathbf{r}_\parallel, z \mid V) \propto & \int_{-\infty}^{+\infty} [f(E_F - eV + \epsilon) - f(E_F + \epsilon)] \\
& \times n(\mathbf{r}_\parallel, z \mid E_F + \epsilon) d\epsilon \\
= & \int_{-\infty}^{+\infty} g_V(\epsilon) \sum_{\mathbf{k}_\parallel \nu} |\psi_{\mathbf{k}_\parallel \nu}(\mathbf{r}_\parallel, z)|^2 \\
& \times \delta(E_F + \epsilon - \epsilon_{\mathbf{k}_\parallel \nu})\, d\epsilon\,, \qquad (1)
\end{aligned}
$$

whereas $\psi_{\mathbf{k}_\parallel \nu}(\mathbf{r}_\parallel, z)$ is the wave function of the state $|\mathbf{k}_\parallel \nu\rangle$ of the sample at the lateral position $\mathbf{r}_\parallel$ and vertical distance[17] z between the sample and the tip. f is the Fermi function and $g_V(\epsilon)$ is defined as the difference of the Fermi function at $E_F - eV + \epsilon$ and $E_F + \epsilon$. In this paper the temperature has always been chosen as room temperature ($kT = 0.025$ eV). The integrand $n(\mathbf{r}_\parallel, z \mid E_F + \epsilon)$ can be referred to as the local density of states (LDOS) of the sample at the position of the tip atom. The tunneling current is then proportional to the integrated LDOS (ILDOS) of the sample.

In the more general approach of Bardeen,[18] based on time-dependent perturbation theory, the tunneling current is proportional to $|M|^2$, where M is the tunneling matrix element. If we make the approximations that the DOS of the tip and the tunnel matrix element are constant within the energy range of the bias voltage, that the form of the wave function depends only little on the applied bias voltage, and that the tip state is of s-orbital symmetry, then $M \propto \psi$ and one obtains Eq. (1). Although we think that the s-orbital tip model is sufficient for the qualitative understanding of the STM image on the basis of the electronic structure it fails, however, to explain the experimentally observed corrugation amplitude quantitatively. Chen[19] has generalized the s-orbital tip model

to arbitrary orbital symmetries. He derived the so-called *derivative rule*, which relates the tunneling matrix element M for a tip wave function with a particular orbital character to the derivative of the wave function ψ of the sample. For example, $M \propto \partial\psi/\partial z$ for a tip orbital with p_z character and $M \propto \partial^2\psi/\partial z^2 - \kappa^2\psi/3$ for a tip with d_{z^2} character, where κ is the inverse decay length of the wave function into the vacuum (for details see below). We apply the derivative rules directly in *ab initio* calculations in order to estimate the influence of the tip states on the STM image and to compare the calculated corrugation amplitude quantitatively with the experiment.

Under normal tunneling conditions the distance between the outermost tip and surface atom is estimated to 4 to 10 Å. Due to the exponential decay of the wave function into the vacuum the reliable representation of the wave functions in this region of the vacuum is a nontrivial problem. For example in supercell calculations using a plane-wave basis, it is difficult to go beyond 3 to 4 Å. Therefore, we use here the full-potential linearized augmented plane wave (FLAPW) method in film geometry.[20] It is a truly two-dimensional method consisting of a semi-infinite vacuum region, which is solved in real space, and of a finite number of atomic layers to describe the substrate. The vacuum wave function is expanded into basis functions

$$\psi_{\mathbf{k}_\parallel \nu}(\mathbf{r}_\parallel, z) = \sum_n c^n_{\mathbf{k}_\parallel \nu} d^n_{\mathbf{k}_\parallel}(z) \exp[\, i(\mathbf{k}_\parallel + \mathbf{G}^n_\parallel)\mathbf{r}_\parallel], \tag{2}$$

which are two-dimensional (2D) plane waves parallel to the surface and linearized z-dependent basis functions $d^n_{\mathbf{k}_\parallel}(z)$ with

$$d^n_{\mathbf{k}_\parallel}(z) = a^n_{\mathbf{k}_\parallel} u^n_{\mathbf{k}_\parallel}(\epsilon_v, z) + b^n_{\mathbf{k}_\parallel} \dot{u}^n_{\mathbf{k}_\parallel}(\epsilon_v, z). \tag{3}$$

$a^n_{\mathbf{k}_\parallel}$ and $b^n_{\mathbf{k}_\parallel}$ are determined by the continuity of the basis function and its derivative at the vacuum boundary to the film interstitial. The vacuum energy parameter ϵ_v, for which the wave functions are solved is usually positioned in the vicinity of the Fermi energy. The function $u^n_{\mathbf{k}_\parallel}(\epsilon_v, z)$ [and analogously its energy derivative $\dot{u}^n_{\mathbf{k}_\parallel}(\epsilon_v, z)$ not shown here] is the exact numerical solution of the one-dimensional Schrödinger equation to the laterally averaged z-dependent part of the vacuum potential $V(z)$:

$$\left[-\frac{\hbar^2}{2m}\frac{d^2}{dz^2} + V(z) - \epsilon_v + \frac{\hbar^2}{2m}(\mathbf{k}_\parallel + \mathbf{G}^n_\parallel)^2 \right] u^n_{\mathbf{k}_\parallel}(\epsilon_v, z) = 0. \tag{4}$$

This choice of the basis functions is ideally suited to describe the vacuum region as it already includes the exponential decay of the wave functions with respect to the correct potential. The maximal distance in z direction, which we have taken into account, was about 13 Å and by this we could calculate the tunneling current at realistic tip sample separations.

In general, we make use of the fact that the local density of states $n(\mathbf{r}_\parallel, z \mid \epsilon)$ should have the same symmetry as the surface structure. Thus we use the rotational part of the 2D space group operations to form out of plane waves symmetrized plane waves, so-called ''star functions'' $\phi^{2D}_s(\mathbf{r}_\parallel)$. A star function corresponds to a representative reciprocal lattice vector $\mathbf{G}^s_\parallel$, which is equivalent with respect to symmetry operations to a star of reciprocal lattice vectors $\mathbf{G}^n_\parallel$. This allows the restriction of the Brillouin-zone summation over the irreducible part of the two-dimensional Brillouin zone (I2BZ).

The LDOS n in the vacuum region determining the tunneling current in the s-orbital tip-model is written as

$$n(\mathbf{r}_\parallel, z \mid \epsilon) = \sum_s n^s(z \mid \epsilon)\, \phi^{2D}_s(\mathbf{r}_\parallel) \tag{5}$$

with

$$n^s(z \mid \epsilon) = \sum_{\mathbf{k}_\parallel \nu} \delta(\epsilon - \epsilon_{\mathbf{k}_\parallel \nu})\, n^s_{\mathbf{k}_\parallel \nu}(z) \tag{6}$$

and

$$n^s_{\mathbf{k}_\parallel \nu}(z) = \sum_{n,n'} c^n_{\mathbf{k}_\parallel \nu} c^{n'*}_{\mathbf{k}_\parallel \nu} d^n_{\mathbf{k}_\parallel}(z) d^{n'*}_{\mathbf{k}_\parallel}(z)\, \delta(\mathbf{G}^n_\parallel - \mathbf{G}^{n'}_\parallel, \mathbf{G}^s_\parallel). \tag{7}$$

For arbitrary tip orbitals, $d^n_{\mathbf{k}_\parallel}(z)$ in Eq. (7) is replaced by derivatives[21] of $d^n_{\mathbf{k}_\parallel}(z)$ with respect to z according to the derivative rule of Chen.

We explicitly show here the first three star functions, $\phi^{2D}_s(\mathbf{r}_\parallel)$ for a bcc-(110) surface lattice, corresponding to the three smallest stars (s=1,2,3) of reciprocal lattice vectors $\mathbf{G}^s_\parallel$, $\mathbf{G}^{(1)}_\parallel = (0,0)$, $\mathbf{G}^{(2)}_\parallel = (1,\sqrt{2})$, $\mathbf{G}^{(3)}_\parallel = (2,0)$, expressed in units of $\sqrt{2}\pi/a_0$, with a_0 being the lattice constant:

$$\phi^{2D}_1(\mathbf{r}_\parallel) = 1, \tag{8}$$

$$\phi^{2D}_2(\mathbf{r}_\parallel) = \tfrac{1}{2}\,[\cos(\mathbf{G}_{\parallel,1}\mathbf{r}_\parallel) + \cos(\mathbf{G}_{\parallel,2}\mathbf{r}_\parallel)\,], \tag{9}$$

$$\phi^{2D}_3(\mathbf{r}_\parallel) = \cos[\,(\mathbf{G}_{\parallel,1} + \mathbf{G}_{\parallel,2})\,\mathbf{r}_\parallel\,]. \tag{10}$$

$\mathbf{G}_{\parallel,1}$ and $\mathbf{G}_{\parallel,2}$ are the two-dimensional reciprocal lattice vectors

$$\mathbf{G}_{\parallel,1} = \frac{\sqrt{2}\pi}{a_0}(1,\sqrt{2}), \quad \mathbf{G}_{\parallel,2} = \frac{\sqrt{2}\pi}{a_0}(1,-\sqrt{2}). \tag{11}$$

In order to analyze our results in terms of a simplified model we follow Sacks *et al.*[22] by approximating the z dependent part of the vacuum wave function $d^n_{\mathbf{k}_\parallel}(z)$, Eq. (3), by its simplified tail. The vacuum is described by a barrier $V(z) = 0$. Then, the vacuum wave function can be solved exactly and the wave function of energy ϵ will decay inside the barrier as

$$d^n_{\mathbf{k}_\parallel}(z) = \exp(-\kappa^n_{\mathbf{k}_\parallel} z) \tag{12}$$

with z pointing into the barrier and with the decay constant

$$\kappa^n_{\mathbf{k}_\parallel}(\epsilon) = \sqrt{2m|\epsilon|/\hbar^2 + (\mathbf{k}_\parallel + \mathbf{G}^n_\parallel)^2}. \tag{13}$$

The energy ϵ is measured with respect to the vacuum potential at large distance from the surface, which is zero in our

case. We can write the $\mathbf{k}_\parallel$- and $\mathbf{G}_\parallel^s$-resolved contribution to the LDOS for the eigenstate $|\mathbf{k}_\parallel \nu\rangle$ at the energy $\epsilon_{\mathbf{k}_\parallel \nu}$ in the form

$$n^s_{\mathbf{k}_\parallel \nu}(z) = \sum_{n,n'} c^n_{\mathbf{k}_\parallel \nu} c^{n'*}_{\mathbf{k}_\parallel \nu} \exp[-(\kappa^n_{\mathbf{k}_\parallel \nu} + \kappa^{n'}_{\mathbf{k}_\parallel \nu}) z] \times \delta(\mathbf{G}^n_\parallel - \mathbf{G}^{n'}_\parallel, \mathbf{G}^s_\parallel), \tag{14}$$

where ϵ of Eq. (13) is replaced by $\epsilon_{\mathbf{k}_\parallel \nu}$. In this model the electronic structure is contained in the coefficients $c^n_{\mathbf{k}_\parallel \nu}$ and the exponential z-dependent decay into the vacuum is now seen explicitly.

The corrugation amplitude Δz is calculated making use of the observation that the corrugation is in the order of typically $\Delta z \simeq 0.10$ Å for all $\mathbf{r}_\parallel$ within the entire unit cell, which is tiny compared to the average tip-sample distance z_0 of about $z_0 \simeq 5$ Å. We write

$$z(\mathbf{r}_\parallel) = z_0 + \Delta z(\mathbf{r}_\parallel) \tag{15}$$

and linearize the tunneling current $I(\mathbf{r}_\parallel, z(\mathbf{r}_\parallel) \mid V) = I(\mathbf{r}_\parallel, z_0 + \Delta z(\mathbf{r}_\parallel) \mid V)$ around z_0,

$$I(\mathbf{r}_\parallel, z(\mathbf{r}_\parallel) \mid V) \approx I(\mathbf{r}_\parallel, z_0 \mid V) + \left.\frac{\partial I}{\partial z}\right|_{(\mathbf{r}_\parallel, z_0 \mid V)} \Delta z(\mathbf{r}_\parallel) \tag{16}$$

$$\approx I_0(V) + dI(\mathbf{r}_\parallel \mid V) \tag{17}$$

with

$$dI(\mathbf{r}_\parallel) = \nabla_{\mathbf{r}_\parallel} I \Big|_{(\mathbf{r}_\parallel, z_0)} d\mathbf{r}_\parallel + \left.\frac{\partial I}{\partial z}\right|_{(\mathbf{r}_\parallel, z_0)} dz(\mathbf{r}_\parallel). \tag{18}$$

The explicit V dependence in Eq. (18) was dropped for convenience. In the constant current mode the tunneling current (and in the Tersoff-Hamann model the ILDOS) is kept constant

$$I(\mathbf{r}_\parallel, z(\mathbf{r}_\parallel) \mid V) = \int_{-\infty}^{+\infty} g_V(\epsilon) n(\mathbf{r}_\parallel, z(\mathbf{r}_\parallel) \mid E_F + \epsilon) d\epsilon = \text{const}(V) \tag{19}$$

and thus $dI(\mathbf{r}_\parallel) = 0$. Taking Eq. (18) and integrating the local change $dz(\mathbf{r}_\parallel)$ from the position of minimal ILDOS $\mathbf{r}_\parallel^{min}$ to the position of maximal ILDOS $\mathbf{r}_\parallel^{max}$ we obtain the maximum corrugation amplitude:

$$\Delta z = \int_{z(\mathbf{r}_\parallel^{min})}^{z(\mathbf{r}_\parallel^{max})} dz(\mathbf{r}_\parallel) = \int_{\mathbf{r}_\parallel^{min}}^{\mathbf{r}_\parallel^{max}} - \left(\frac{\partial I}{\partial z}\right)^{-1}_{(\mathbf{r}_\parallel, z_0)} \nabla_{\mathbf{r}_\parallel} I(\mathbf{r}_\parallel, z_0)\, d\mathbf{r}_\parallel. \tag{20}$$

Replacing the tunneling current I by the ILDOS according to Eq. (19), use the expansion of the LDOS $n(\mathbf{r}_\parallel, z)$ in terms of star functions $\phi_s^{2D}(\mathbf{r}_\parallel)$ [Eq. (5)], approximate the summation over the stars by the leading star contributions, since higher star coefficients become quickly negligible, which is $s=1$ for $\partial I/\partial z$ [which means we replace $\partial I/\partial z$ at $(\mathbf{r}_\parallel, z_0)$ by an $\mathbf{r}_\parallel$ independent $\partial I/\partial z$ at (z_0) for all $\mathbf{r}_\parallel$ and pull this term in front of the integral], and $s=2,3$ for $\nabla_{\mathbf{r}_\parallel} I$, we arrive at our final result for the corrugation amplitude:

$$\Delta z(z_0 \mid V) \approx S \frac{\sum_{s=2,3} \Delta \phi_s^{2D} \int_{-\infty}^{+\infty} g_V(\epsilon) n^s(z_0 \mid E_F + \epsilon)\, d\epsilon}{\int_{-\infty}^{+\infty} g_V(\epsilon) 2\kappa^{(1)}_{\mathbf{k}_\parallel = \mathbf{0}}(\epsilon) n^{(1)}(z_0 \mid E_F + \epsilon)\, d\epsilon}. \tag{21}$$

In this equation, $\Delta \phi_s^{2D}$ is the difference of the star function at the location of the maximum and the minimum ILDOS $I(\mathbf{r}_\parallel, z(\mathbf{r}_\parallel) \mid V)$:

$$\Delta \phi_s^{2D} = \phi_s^{2D}(\mathbf{r}_\parallel^{max}) - \phi_s^{2D}(\mathbf{r}_\parallel^{min}). \tag{22}$$

In order to calculate the derivative with respect to z the z dependence of the first star coefficient $n^{(1)}(z \mid \epsilon)$ has been approximated by $n^{(1)}(z \mid \epsilon) \propto \exp(-2\kappa^{(1)}_{\mathbf{k}_\parallel = \mathbf{0}} z)$. κ is the energy-dependent decay length: $\kappa^{(1)}_{\mathbf{k}_\parallel = \mathbf{0}} = [2m|\epsilon|/\hbar^2]^{-1/2}$. The $\mathbf{k}_\parallel$ dependence of κ has been approximated by $\mathbf{k}_\parallel = \mathbf{0}$. We will discuss below that this is a good approximation, since $\mathbf{k}_\parallel = \mathbf{0}$ dominates the $n^{(1)}$ contribution to the tunneling current. The origin of the coordinate system for the $\mathbf{r}_\parallel$ integration is located at the position of the surface atom and $\mathbf{r}_\parallel^{max}$ and $\mathbf{r}_\parallel^{min}$ are taken from the positive quadrant of the 2D surface unit cell. In order to suffice our choice of definition, that the corrugation amplitude is positive if the tip-sample distance at the position of the atom is larger than at the hollow site, an additional sign was introduced in Eq. (21):

$$S = \text{sgn}\left[\int_{-\infty}^{+\infty} g_V(\epsilon) n^{(2)}(z_0 \mid E_F + \epsilon)\, d\epsilon\right]. \tag{23}$$

S is thus the sign of the integrated second star coefficient. This definition makes use of the fact, that the second star function has a maximum at the site of the atom and a minimum at the hollow site taken our definition of star functions. A negative sign of the second star coefficient turns the maximum to a minimum and *vice versa*. If the second star coefficient becomes very small then this definition is arbitrary since the corrugation pattern does not look like the second star function any more.

The quality of Eq. (21) has been tested calculating $n(\mathbf{r}_\parallel, z)$ on a fine z grid in real space and evaluate Δz directly from the condition that $n(\mathbf{r}_\parallel, z(\mathbf{r}_\parallel)) = \text{const}$. The two different approaches are in good agreement although the evaluation of Eq. (21) is much faster.

III. COMPUTATIONAL DETAILS

The electronic structure of the W(110) surface has been calculated with the full-potential linearized augmented plane-wave method[20] in film geometry. The calculations apply density functional theory[23] in the local (spin) density approximation of Barth and Hedin[24] using the parametrization by Moruzzi, Janak, and Williams.[25] A film consisting of 11 layers has been chosen to simulate the surface using the experimental W lattice constant ($a_0 = 5.972$ a.u.). No vertical relaxation of the surface has been included, since it is experimentally known to be less than 2%.[26] The valence electrons are treated in the scalar-relativistic approximation while the core electrons are calculated full relativistically. The basis set used for the valence states consists of about 100 aug-

mented plane waves per atom in the unit cell. Nonspherical terms in the potential, charge density and wave functions are expanded within the muffin-tin spheres with radius $R_{MT}=2.456$ a.u. up to $l_{max}\leqslant 8$. Integrations over the 2D Brillouin zone (BZ) have been performed with the special $\mathbf{k}_{\|}$ method.[27] The self-consistent electronic structure was determined with 36 $\mathbf{k}_{\|}$ points in the I2BZ. The ILDOS resolved over the 2D BZ has been analyzed using 630 $\mathbf{k}_{\|}$ points in the I2BZ. All star coefficients and by this also the STM images and corrugation amplitudes were calculated on this $\mathbf{k}_{\|}$ point basis.

Calculations of Ta(110) were performed with the same parameters as in the case of W(110) using the experimental lattice constant of Ta ($a_0=6.25$ a.u.) and a muffin-tin radius of $R_{MT}=2.65$ a.u.

Calculations of ferromagnetic bcc Fe(110) were carried out employing the local spin density approximation. The Fe(110) surface was described by a 15 layer Fe film and the theoretically determined lattice constant of $a_0=5.23$ a.u., determined by minimization of the total energy with respect to the lattice constant. A muffin-tin radius of $R_{MT}=2.151$ a.u. was chosen. All other parameters are identical to those of the W(110) calculation.

The vacuum energy-parameter ϵ_v was set close to the Fermi energy E_F. We tested the influence of the energy parameter on the LDOS at the position of the tip ($z_0=5$ Å). Setting ϵ_v to the Fermi energy E_F did not change the LDOS significantly.

IV. EXPERIMENTAL DETAILS

The experimental data were measured with a commercial ultra-high-vacuum (UHV) compatible scanning tunneling microscope (Micro-STM, Omicron) operated in a home-built UHV chamber with a base pressure in the low 10^{-11} torr range. The chamber was equipped with facilities for substrate heating by electron bombardment and a combined LEED/Auger-optic for checking surface crystallographic order and cleanliness of the sample prior to imaging with the STM. We prepared the W(110) single crystal by cycles of heating in an oxygen atmosphere ($p_O=1\times10^{-7}$ torr) for 30 min and subsequent flashing up to 2600 K.[28] Imaging was carried out in constant current mode at room temperature. Typically, when trying to obtain atomic resolution images we took 50 Å scans with a 0.1 Å per pixel increment. The piezotube scanner was calibrated on highly orientated pyrolytical graphite (HOPG) and Si(111)-7×7 *ex situ* and *in situ*, respectively.

V. RESULTS AND DISCUSSION

A. STM images

Figure 1(a) shows a 33×25 Å^2 constant current topography of the W(110) surface taken at a bias voltage of about +40 mV and a tunneling current of 10 nA. This image shows atomic scale corrugation appearing as an equidistant array of black interstices and nets of protrusions. The length scale and orientation of the arrays are consistent with a $p(1\times1)$ unit cell of W(110), which suggests that the observed corrugations are associated with the positions of the W atoms. The features of this image where typical of those taken at different locations on the surface.

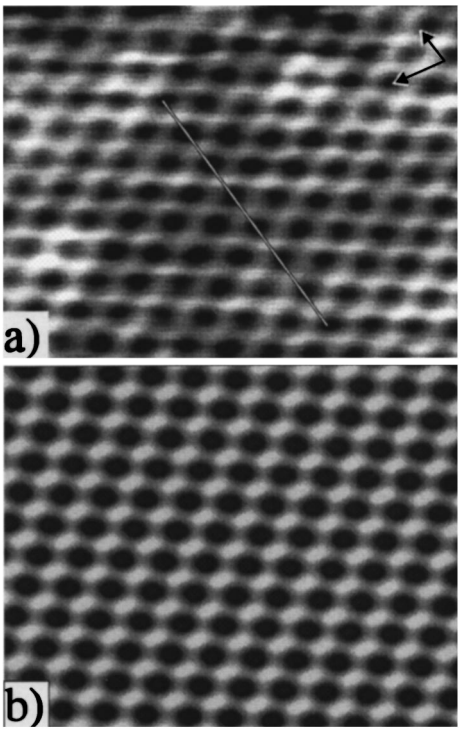

FIG. 1. Comparison of experimental and calculated STM image. (a) Atomically resolved clean W(110) surface at a bias voltage of about 40 mV and a tunneling current of about 10 nA. The scan area is 33 Å × 25 Å. (b) Calculated ILDOS at a distance of 5 Å above the surface atoms in an energy range equivalent to (a). Line section as indicated in (a) is presented in Fig. 3.

Figure 1(b) displays the calculated ILDOS at a distance of 5 Å from the surface atoms in the energy range of (E_F,E_F +50 meV). This tip-surface distance is a typical value for which little tip-surface interactions are expected. We find good agreement between experiment and theory. Both images show a pattern of dark spots with the symmetry of the 2D surface unit cell. Looking more carefully one also finds a pattern of bright spots, with the same symmetry, which are connected by feeble, fuzzy lines. Although the atomic resolution of the STM image can already be deduced by the symmetry and lateral scale of the pattern, it is *a priori* not clear whether the bright or the dark spots correspond to the atomic sites. From the calculated image we find that at this particular bias voltage the interpretation of the STM image is indeed in line with the intuitive assumption that large tunnel current (bright spots) corresponds to the atomic sites. The dark spots correspond to the hollow sites of the (110) surface unit cell. Images at other particularly negative bias voltages could not be obtained in this experiment.

B. Voltage-dependent corrugation reversal

On the other hand, STM images were recalculated for different bias voltages. We found a surprising result: depending on the bias voltage we predict that sites of high tunneling current correspond to the hollow sites or interstitial sites, respectively, and sites of low tunneling current correspond to the atom positions, e.g., *vice versa* to the results of Fig. 1.

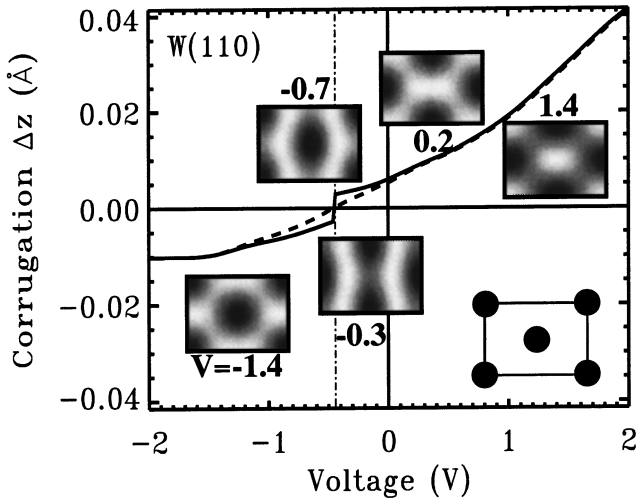

FIG. 2. Dependence of the corrugation amplitude Δz on the bias voltage of the calculated STM image of W(110). Insets show the surface unit cell (bottom right) with atomic sites marked by dots and typical STM images calculated for different bias voltages V. The full line displays $\Delta z = z_{max} - z_{min}$, calculated by Eq. (21), between the lateral points $\mathbf{r}_\parallel$ of maximum and minimum corrugation within the unit cell. The dashed line displays $\Delta z = z_{atom} - z_{hollow}$, the corrugation measured between the position of the atom and the hollow site. All results are calculated at a distance of $z_0 = 4.6$ Å. Area of dark gray scale means small tunneling current.

This corrugation reversal is documented in Fig. 2 at a distance $z_0 = 4.6$ Å from the surface. The maximum corrugation amplitude $\Delta z = z_{max} - z_{min}$ between the lateral points $\mathbf{r}_\parallel^{max}$ and $\mathbf{r}_\parallel^{min}$ of maximum and minimum tip-sample distances is plotted as function of the applied bias voltage V together with the corrugation amplitude $\Delta z = z_{atom} - z_{hollow}$ measured as difference between the tip-sample distances at the position of the atom and the hollow site.

In the case of $V > 0$, corresponding to the bias voltage in Fig. 1, we determined a positive corrugation amplitude of the order of 0.01 Å, which rises at higher voltages up to 0.04 Å. The positive sign of the corrugation amplitude means that atoms are imaged as protrusions (normal image) and representative topography images of the rectangular surface unit cell are shown in Fig. 2 as insets for voltages of 0.2 and 1.4 V.

In the case of high negative voltages ($V < -0.9$ V) we find that the image is reversed and hence the sign of the corrugation amplitude is negative. The absolute value is of the same order as in the positive voltage regime. A typical image is shown as an inset in Fig. 2 ($V = -1.4$ V). Comparing the insets at positive voltage and high negative voltage, the effect of image reversal is quite apparent (see the 2D unit cell as reference).

In the intermediate voltage regime, in which the corrugation reversal occurs, the images display a pattern of bent stripes parallel to the short side of the rectangular unit cell. Starting from a voltage with a normal image (i.e., $+1.4$ V) and reducing the bias voltage continuously there is a gradual change and absolute maxima change to local maxima at the positions of the atoms in the intermediate voltage regime. At a voltage of about $V = -0.4$ V even the local maxima have disappeared. The change is also pointed out by the dashed line in Fig. 2, which shows the difference Δz between an atom position and a hollow site of the unit cell and does not coincide with the corrugation amplitude. The analogous discussion occurs starting with a reversed image at large negative voltages, but in this case absolute maxima change to local maxima at the hollow position (see inset in Fig. 2 for $V = -1.4$ V and $V = -0.7$ V).

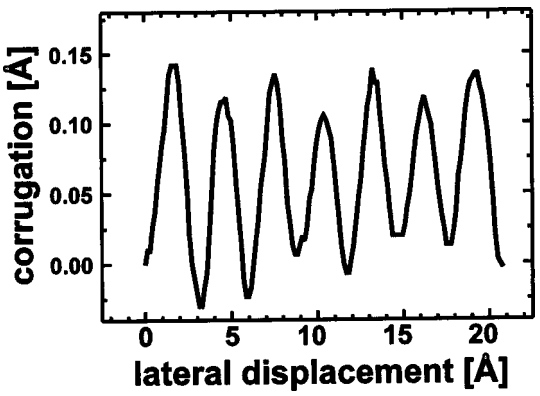

FIG. 3. A corrugation profile taken by a line scan along the [001] direction of the W(110) surface as indicated by a straight line in Fig. 1(a) using scanning parameters as given in Fig. 1.

The voltage, which can be identified as the border between normal and reversed image, is about -0.4 V. However, this is not an absolute number since it changes with the distance z_0, which corresponds experimentally to the chosen constant current. The trend is that for separations larger than $z_0 = 4.6$ Å, the critical voltage rises linearly. At a distance of 7.2 Å it is equal to 0 V.

Obviously, these observations are in contradiction to conventional wisdom that on metal surfaces there is a one to one correspondence between high tunnel current and atom positions. The effect of image reversal makes the determination of atomic sites by the STM image rather difficult.

Finally we would like to stress one more point: In the transition regime of image-reversal at bias voltages between -0.7 V and 0 V, the corrugation amplitude becomes extremely small and we speculate that this might be the origin of the experimental difficulties in resolving the W(110) surface with atomic resolution at negative bias voltage.

C. Corrugation amplitude

Figure 3 shows a typical corrugation profile taken along the [001] direction of the W(110) surface as indicated by a straight line in Fig. 1(a). The experimental value for the corrugation amplitude is about 0.13 Å. This is about one order of magnitude larger than the theoretically determined corrugation in Fig. 2, which is of the order of 0.01 Å at a distance z_0 from the surface of 4.6 Å.

We attribute this tiny and in reality by STM nondetectable corrugation amplitude to the application of the Tersoff-Hamann model,[2] which is based on *s*-like tip wave functions. As described above, Chen[19] has extended this model to arbitrary tip orbitals. We have applied the *derivative rule* to the calculated STM image of Fig. 1(b) and extracted new corrugation amplitudes, using the same procedure as before. In addition to the *s*-orbital, which corresponds to the description of Tersoff and Hamann, the tip states with p_z and d_{z^2} char-

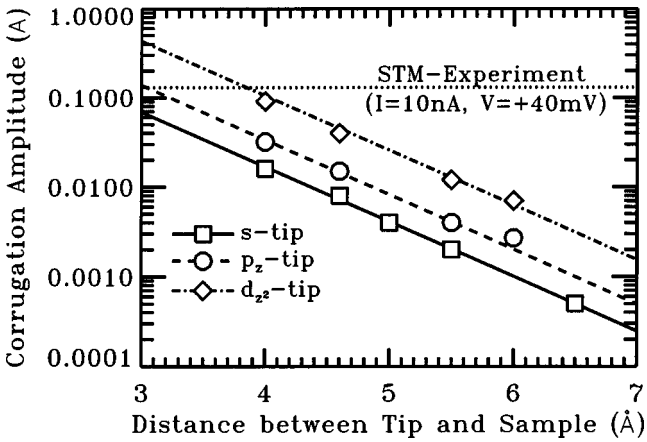

FIG. 4. Corrugation amplitude as function of the tip-sample distance for three different orbital symmetries of the tip state. Using Chen's derivative rule (Ref. 19) the corrugation amplitudes for *s*-, p_z-, and d_{z^2}-type tip orbitals have been calculated at a bias voltage of $+0.1$ V. The experimental corrugation amplitude obtained from the STM-image of Fig. 1(a) is given by the horizontal dotted line. Symbols indicate calculated values. The full line is a linear interpolation of the values calculated for an *s*-type tip. The dashed and dotted-dashed lines are given by the interpolated values of the *s*-type tip multiplied by Chen's enhancement factors (Ref. 19) for a p_z and d_{z^2} tip, respectively.

acter are considered. Figure 4 shows the corrugation amplitude as function of the tip-sample distance for the three different tip orbitals. The corrugation amplitudes were calculated at different tip-sample distances for a fixed bias voltage of $+0.1$ V. The linear scaling of the corrugation amplitudes as function of the tip-sample distance in the semilogarithmic plots describes the exponential decay of the tunneling current with the distance. Comparing the corrugation amplitudes of a p_z- or d_{z^2}-state tip with that of an *s*-state one, the amplitudes are larger by factors of 2 or 6.25, respectively, as predicted by Chen's derivative rule.[19] These results are consistent with the experimentally measured corrugation amplitude (cf. Fig. 3) of 0.13 Å, added in Fig. 4 as dotted horizontal line, for a tip-sample separation of about 4 Å. This distance is already quite small, but it is consistent with an estimation of the experimental tip-sample separation by means of the tunnel conductance:

$$G=\frac{I}{U}=\frac{2e^2}{h}\exp[-2\kappa(z-z_{contact})]. \tag{24}$$

In Eq. (24) we make the assumption that the tunnel conductance becomes equal to the conductance quantum at (single atom) contact $z=z_{contact}$ and that it decreases exponentially with increasing distance from the surface. Applied to the tunneling conditions of Fig. 1(a), this leads to a value of $z-z_{contact}=2.4$ Å. Taking $z_{contact}$ as the lattice plane separation in tungsten of 1.6 Å [$\langle 100\rangle$ directions] to 2.2 Å [$\langle 110\rangle$ directions] one ends up with a tip-sample separation of 4.0–4.6 Å. This result is in accordance to our estimation comparing the calculated and measured corrugation amplitude.

The orbital character of the tip state depends much on the tip material used. Experiments discussed in this paper have been carried out with W tips. For W tip atoms the tunneling is mostly due to *d* electrons at the Fermi energy. This has also been confirmed by electronic structure calculations of Ohnishi *et al.*[29] on W clusters, which makes the assumption of d_{z^2} rather realistic.

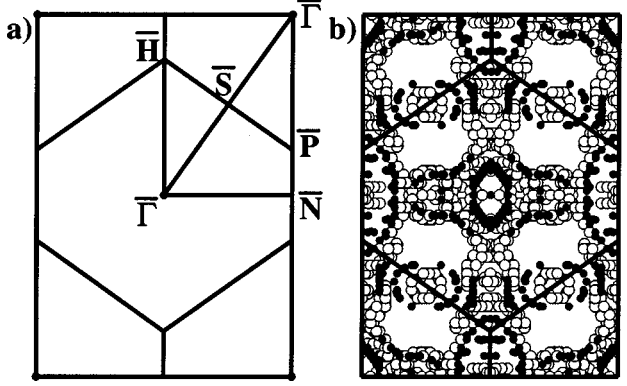

FIG. 5. Fermi surface of W(110). (a) 2D Brillouin zone corresponding to the centered rectangular unit cell of bcc transition-metal (110) surfaces [e.g., W(110)]. (b) States of W(110) at the Fermi energy. Open circles mark bulk states while filled circles represent surface states or resonances with a localization (expectation value) of either more than 10% within the vacuum region or more than 45% within the muffin-tin spheres of the surface atoms including the vacuum region or more than 65% within the surface atoms, subsurface atoms and the vacuum region.

We may draw one important conclusion from this investigation: The corrugation reversal shown in Fig. 2, and calculated for an *s*-state tip, should be also scaled-up by the enhancement factor[19] and thus should be detectable by STM experiments. Although more realistic tip orbitals magnify the corrugation amplitude we found, however, that the STM images obtained from p_z or d_{z^2} state tip orbitals do not differ qualitatively from the *s*-tip images. Therefore, we can safely restrict the further discussion and analysis on the corrugation reversal to the model of Tersoff and Hamann.

D. Analysis of corrugation reversal

To give an explanation of the image reversal on the basis of the electronic structure we start with the Fermi surface of W(110) as displayed in Fig. 5. Figure 5(a) shows the centered rectangular 2D Brillouin zone (BZ) of the bcc (110) surface and in Fig. 5(b) calculated electronic states at the Fermi energy are marked. Small open circles distinguish bulklike states from surface localized states represented by full dots. One finds three surface resonance bands and a surface-state band which have also been studied experimentally by photoemission.[30] The experimentally observed surface resonances and surface state at the Fermi surface were explicitly mapped[30] over the 2D BZ and a comparison shows a good agreement to our calculation (cf. Fig. 5). The surface state surrounds the $\bar{S}$ point of the Brillouin zone while one resonance is around $\bar{\Gamma}$, and around $\bar{N}$, and a third one is stretching along the axes $\bar{\Gamma}\bar{H}$ and $\bar{\Gamma}\bar{N}$. In order to see the dispersion of these different surface localized states Fig. 6 shows the band structure in $\bar{\Gamma}\bar{S}$ direction. One recognizes the surface state located in an energetic gap of bulk bands as well as two types of resonances. The surface-state band has

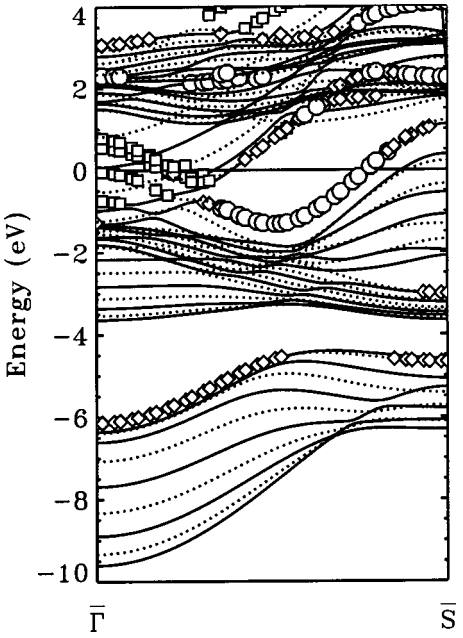

FIG. 6. Calculated surface band structure of W(110) along the $\overline{\Gamma S}$ direction of the Brillouin zone. States marked with square, dot, or diamond are localized with more than 5% in the vacuum, more than 60% within the vacuum plus the muffin-tin sphere of the surface atom, or more than 70% within the vacuum plus the muffin-tin spheres of the surface and subsurface atoms, respectively. The Fermi energy E_F defines the energy zero.

its energetic minimum at -1.3 eV and from a more detailed analysis it can be concluded that its character changes from predominantly *d* character at the minimum to a *p*-type state at the zone boundary. This change occurs gradually and states near the Fermi energy have comparable contributions of both types with a small admixture of *s* electrons. While the resonance around $\overline{\Gamma}$ exhibits a rather flat dispersion, the resonance crossing the Fermi energy approximately halfway to $\overline{S}$, rises quite steeply. Thus there is a considerable number of possible electronic states responsible for the observed phenomena and one has to understand the relative importance of these states as well as their quantitative contribution to the corrugation inversion. In order to find those states, which contribute most to the corrugation in STM images we are looking at the *z* dependence of the wave functions at different points in reciprocal space. Following Sacks *et al.*[22] we begin the analysis in terms of a simplified model introduced by Eqs. (12)–(14). In this model we can see that the $\mathbf{k}_\parallel$- and $\mathbf{G}_\parallel^s$-resolved contribution to the surface topography at the surface plane $z=0$ is detected at the distance *z* after $\mathbf{k}_\parallel$- and $\mathbf{G}_\parallel^s$-dependent weighting expressed by Eq. (12). Consequently, waves with the smallest lattice vectors $\mathbf{G}_\parallel^s$ and the highest energy ϵ will reach out furthest into the vacuum and contribute most to the STM image. The $\mathbf{k}_\parallel$-dependent filtering effect of $\exp(-\kappa_{\mathbf{k}_\parallel}^n z)$ on $n_{\mathbf{k}_\parallel \nu}^s(z)$ is analyzed graphically in Figs. 7(a)–7(c) for the three smallest stars ($s=1,2,3$) of reciprocal lattice vectors $\mathbf{G}_\parallel^s$. Figures 7(a)–7(c) display the

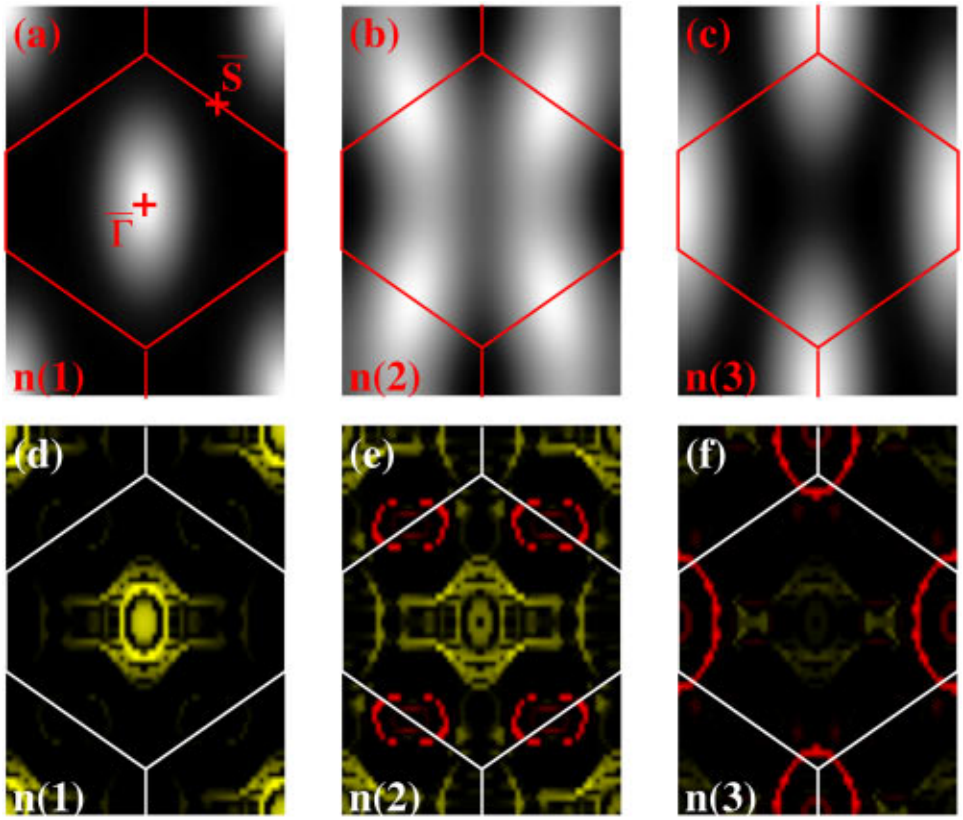

FIG. 7. (Color) Star coefficients in $\mathbf{k}_\parallel$ space at a tip-sample distance z_0 of 4.6 Å. Panels (a) to (c) show the first three star coefficients decay function as calculated by Eq. (14) with $E_F=-5.69$ eV and (d) to (f) show the first three star coefficients of the FLAPW calculation for W(110) in the energy range $(E_F-0.2$ eV $, E_F)$. Images (d) to (f) have been calculated using 630 $\mathbf{k}_\parallel$ points in the I2BZ. Yellow shows positive coefficient values while red marks negative values.

exponential decay of $n^s_{\mathbf{k}_\parallel}(z_0 \mid E_F)$ in terms of gray scale plots over the 2D Brillouin zone calculated for the Fermi energy, $\epsilon = E_F$, at a tip-sample distance of $z_0 = 4.6$ Å. In these plots the electronic structure has been explicitly ignored by replacing in Eq. (14) all coefficients $c^n_{\mathbf{k}_\parallel \nu}$ by a constant and replacing $\kappa^n_{\mathbf{k}_\parallel \nu}$ by $\kappa^n_{\mathbf{k}_\parallel}(E_F)$. We used $E_F = -5.69$ eV as calculated for our W(110)-film. These results need to be compared to Figs. 7(d)–7(f), which show the actual coefficients $n^s_{\mathbf{k}_\parallel \nu}(z_0)$ for the first three stars, including the electronic structure, calculated according to Eq. (7) by FLAPW calculations in the energy interval $(E_F - 0.2$ eV,$E_F)$. On the basis of Fig. 7 we can discuss the importance of various contributions to the tunneling current over the $\mathbf{k}_\parallel$ space.

The first term $n^{(1)}_{\mathbf{k}_\parallel}$ corresponding to $\mathbf{G}^{(1)}_\parallel = \mathbf{0}$ leads to an $\mathbf{r}_\parallel$ independent, i.e., laterally constant contribution to the tunneling current [cf. Eq. (8)]. $n^{(1)}_{\mathbf{k}_\parallel}$ is always positive. It does not make any contribution to the corrugation pattern but it adds to the total tunneling current (total LDOS) and thus it is important in scanning tunneling spectroscopy. In Fig. 7(a) one concludes that this star coefficient is dominated by states near the center of the BZ as is commonly accepted. Comparing Fig. 7(a) to Fig. 7(d), it is clear that the particular electronic structure of the surface still leads to some deviation of the simple picture. One can recognize the surface resonance around $\overline{\Gamma}$ as well as a part of the resonance which stretches along the axes of $\mathbf{k}_\parallel$ space (see Fig. 5 for comparison). The area in the BZ which is of importance for $n^{(1)}_{\mathbf{k}_\parallel}$ is thus still influenced by the particular electronic structure. The decay of the second star coefficient $n^{(2)}_{\mathbf{k}_\parallel}$ of the LDOS is displayed in Fig. 7(b). The STM topography pattern resulting from the second star function [see Eq. (9)] depends on the sign of the star coefficient and contributes to corrugation or anticorrugation as seen in Fig. 2 for voltages $V = +1.4$ V or $V = -1.4$ V, respectively. One finds that in this case the main contribution results from states around $\overline{\mathrm{S}}$. From Fig. 7(e) we analyze the contribution to the STM image made by different states in the BZ. Figure 7(e) displays positive $n^{(2)}_{\mathbf{k}_\parallel}$ coefficients in yellow and red for coefficients with negative sign. Now one can easily understand the different role of the surface resonance and the surface state on the corrugation. We find that all bulk states and all surface resonances have positive $n^{(2)}_{\mathbf{k}_\parallel}$ coefficients and contribute to a normal STM image, consistent with the general wisdom for metal surfaces that electrons try the screen the positive charge of the nucleus and the STM topography and the atom position should coincide. The surface states located around $\overline{\mathrm{S}}$ are the only states with negative $n^{(2)}_{\mathbf{k}_\parallel}$ and are the single source of the anticorrugation of the STM image. In addition the negative $n^{(2)}_{\mathbf{k}_\parallel}$ contributes to the total $n^{(2)}$ by a large weighting factor because of its position close to $\overline{\mathrm{S}}$ while the resonances are of rather small value due to the little weight of $n^{(2)}_{\mathbf{k}_\parallel}$ at the $\overline{\Gamma}$ or $\overline{\mathrm{H}}$ point. The resonance along the axes $\overline{\Gamma}\overline{\mathrm{H}}$ and $\overline{\Gamma}\overline{\mathrm{N}}$ contributes the highest values among the normal states.

The actual STM image for a chosen bias voltage depends upon the integral value of the second star coefficient of

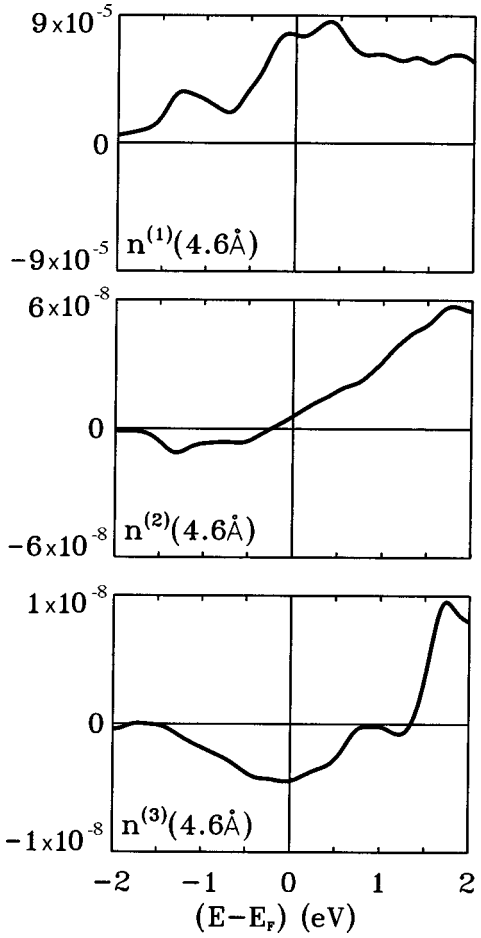

FIG. 8. Star coefficients integrated over the 2D Brillouin zone as a function of energy at $z_0 = 4.6$ Å. (a) $n^{(1)}(z|\epsilon)$, (b) $n^{(2)}(z|\epsilon)$, and (c) $n^{(3)}(z|\epsilon)$. $n^{(1)}(z|\epsilon)$ is always positive since it resembles the LDOS. The sign of $n^{(2)}(z|\epsilon)$ decides whether the STM image displays a corrugation or anticorrugation pattern. The value of $n^{(3)}(z|\epsilon)$ is non-neglectable only in the energy range that shows the change of sign for $n^{(2)}(z|\epsilon)$. Compare Fig. 2.

the LDOS over the 2D BZ. This quantity, $n^s(z_0 \mid \epsilon)$, is displayed in Fig. 8 for the first three star coefficients as a function of energy at a tip-sample distance of $z_0 = 4.6$ Å. We see $n^{(1)}(\epsilon)$ is always positive, since it represents the total charge density integrated over the 2D unit cell. The second star coefficient of the LDOS $n^{(2)}(\epsilon)$ is three orders of magnitude smaller than $n^{(1)}(\epsilon)$ and changes sign at an energy of about -0.2 eV. Thus for energies below -0.2 eV the negative contribution of the surface states is higher in absolute value than the contribution of all other states, which is positive. Since the tunneling current at a certain bias voltage V is given by an energy integral of the LDOS between E_F and $E_F + eV$ [Eq. (1)], the corrugation does not change its sign until a voltage of -0.4 V is reached (see Fig. 2). Then the positive values of $n^{(2)}$ states between $E_F - 0.2$ eV and E_F are compensated by negative values between $E_F - 0.4$ eV and $E_F - 0.2$ eV. Reducing the applied voltage below -0.4 V results then in an image reversal. A maximal negative value of $n^{(2)}(z \mid \epsilon)$ is reached at -1.3 eV, which is the minimum of the surface state band (Fig. 6) consistent with the interpretation that the surface state is responsible for anticorrugation. The change in sign of the second star coefficient and its

rise for energies above E_F is due to the competition between the surface state and the resonance. Finally the third star coefficient is plotted in Figs. 7(c) and 7(f). The z-dependent $\mathbf{k}_\parallel$-point filtering shown in Fig. 7(c) projects out states near the $\bar{\mathrm{N}}$ point. The emphasis on these states also becomes evident in the plots including the electronic structure [Fig. 7(f)]. One observes the strong influence of the resonance around the $\bar{\mathrm{N}}$ point on this star coefficient of the LDOS. The third star coefficient can become positive or negative, but the third star function [see Eq. (10)] is simply a cosine function in the $[1\bar{1}0]$ direction of the surface and hence it is not responsible for the effect of corrugation reversal. Nevertheless, the actual FLAPW calculation demonstrates that $n^{(2)}$ and $n^{(3)}$ can be of comparable value. This happens for the energy regime between -0.4 and 0 eV, when the second star coefficient becomes quite small (see Fig. 8) or zero due to the compensation between the surface state and the resonance. In this regime the superposition of the star function $\phi_2^{2D}(\mathbf{r}_\parallel)$ and $\phi_3^{2D}(\mathbf{r}_\parallel)$ leads to new images exhibiting patterns of bent stripes from the cosine function $\phi_3^{2D}(\mathbf{r}_\parallel)$ (see the patterns in Fig. 2 at voltages -0.7 V and -0.3 V). Stars of even higher order do not contribute significantly anymore because the average value of the star coefficients n^s decreases exponentially with the length of the star vector as can be concluded from equation (14) and is also evident from Fig. 8. In Fig. 9 the charge density contours in real space of typical surface states and surface resonances along the $\bar{\Gamma}\bar{\mathrm{H}}$ and $\bar{\Gamma}\bar{\mathrm{N}}$ lines are displayed. Figures 9(a) and 9(b) show cross sections through the W(110) film of states lying on the surface-state band. One finds a charge density between surface atoms which spills into the vacuum and causes the anticorrugated image. The behavior of the resonance states shown in Figs. 9(c) and 9(d) is quite different. The d_{xz}- and d_{z^2}-type states lead to vacuum LDOS located at the atom and thus to a normal STM imaging of atomic sites.

In order to understand the formation of the charge density contour of the surface state as exhibited in Figs. 9(a) or 9(b) and the surface state itself from the bulk bands we follow the formation of the W(110) surface from the bulk by pulling apart the W bulk in discrete steps long the [110] direction. We have chosen a (110) unit cell of 4 (110) planes in z direction and increased the separation between these unit cells by 0.5, 1.0, and 2.5 Å along the z direction starting from the bulk separation. At each separation we calculated the projected band structure and confirmed that the surface-state band described above is a split-off state from binding bulk states and is lifted in energy. The evolution of the charge density contour associated with a particular surface state along with the formation of the surface is shown in Fig. 10 for the different unit-cell separations. In the bulk, the state under discussion is a bonding state with bonding charges between the atoms along the short side of the centered rectangular [the $\langle 001\rangle$ directions] unit cell of the bcc (110) surface. Along the long side of the unit cell [the $\langle 110\rangle$ directions] there are charge density zeros between the atoms and it is thus an antibonding state along the long side of the unit cell and perpendicular to the surface. As the surface is formed, the bond strength between atoms at the forming surface is increased, the symmetry of the forming surface state changes, the hybridization of this state with the underlying

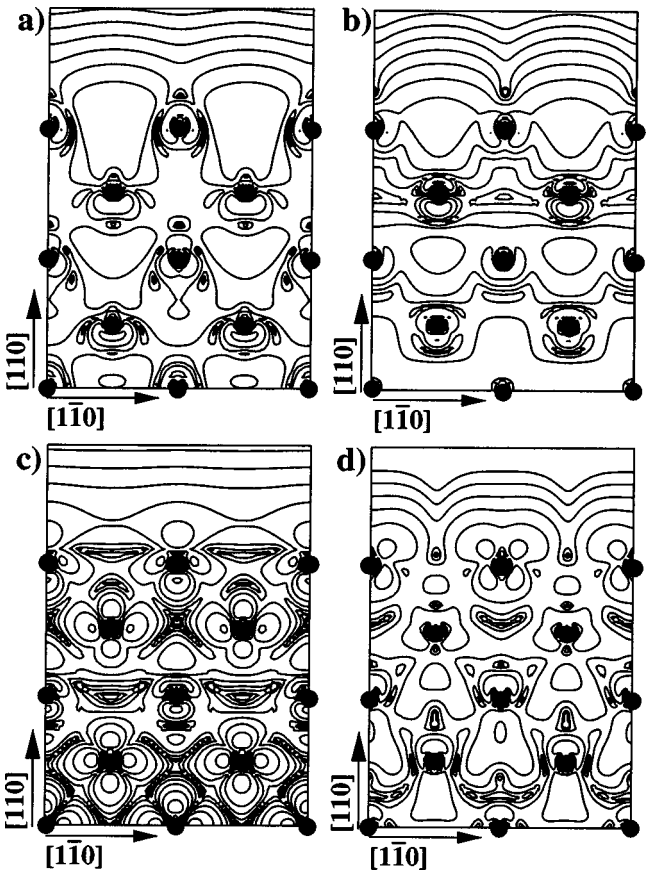

FIG. 9. Single-state valence charge-density contour maps, $n_{\mathbf{k}_\parallel \nu}(\mathbf{r})$ for W(110) on the (001) plane. Contours start from 10^{-7} electrons/(a.u.)^3 and increase by a factor of 4. (a) and (b) show plots for states on the surface-state band at $\mathbf{k}_\parallel=(0.35,0.39\sqrt{2})\pi/a\sqrt{2}$, $\epsilon_\nu=-0.05$ eV and $\mathbf{k}_\parallel=(0.58,0.38\sqrt{2})\pi/a\sqrt{2}$, $\epsilon_\nu=-0.11$ eV, respectively. (c) and (d) show plots for states on the surface-resonance bands at $\mathbf{k}_\parallel=(0.15,0.18\sqrt{2})\pi/a\sqrt{2}$, $\epsilon_\nu=+0.04$ eV and $\mathbf{k}_\parallel=(0.15,0.61\sqrt{2})\pi/a\sqrt{2}$, $\epsilon_\nu=+0.04$ eV, respectively. Atom positions are marked by filled circles.

substrate decreases and leads to a dehybridization of subsurface charge, the charge density of the so formed surface state releases energy by spilling out into the vacuum and causes the anticorrugation. The behavior of the surface state reminds at the formation of dangling bond states of covalently bonded semiconductors with direction sp^3 hybrids, which are also responsible for anticorrugation. For the surface resonance states (not shown here) the picture is quite different. The charge density is located at the atom and the symmetry does not change by the formation of the surface and a resonance state supports a normal image. In order to confirm our interpretation of the formation of the surface-state band as being partly due to the dehybridization of subsurface states in favor to the surface state, which gives the characteristic charge density features leading to anticorrugation in STM images, we also calculated a free monolayer of W(110). In that case we expect to find no states which exhibit an anticorrugation image since there is no subsurface layer. The band structure of the monolayer is presented in Fig. 11. Comparing this band structure with the 11-layer calculation of Fig. 6 one notices that the surface-state band with its characteristic energy minimum in the middle of the $\bar{\Gamma}\bar{\mathrm{S}}$

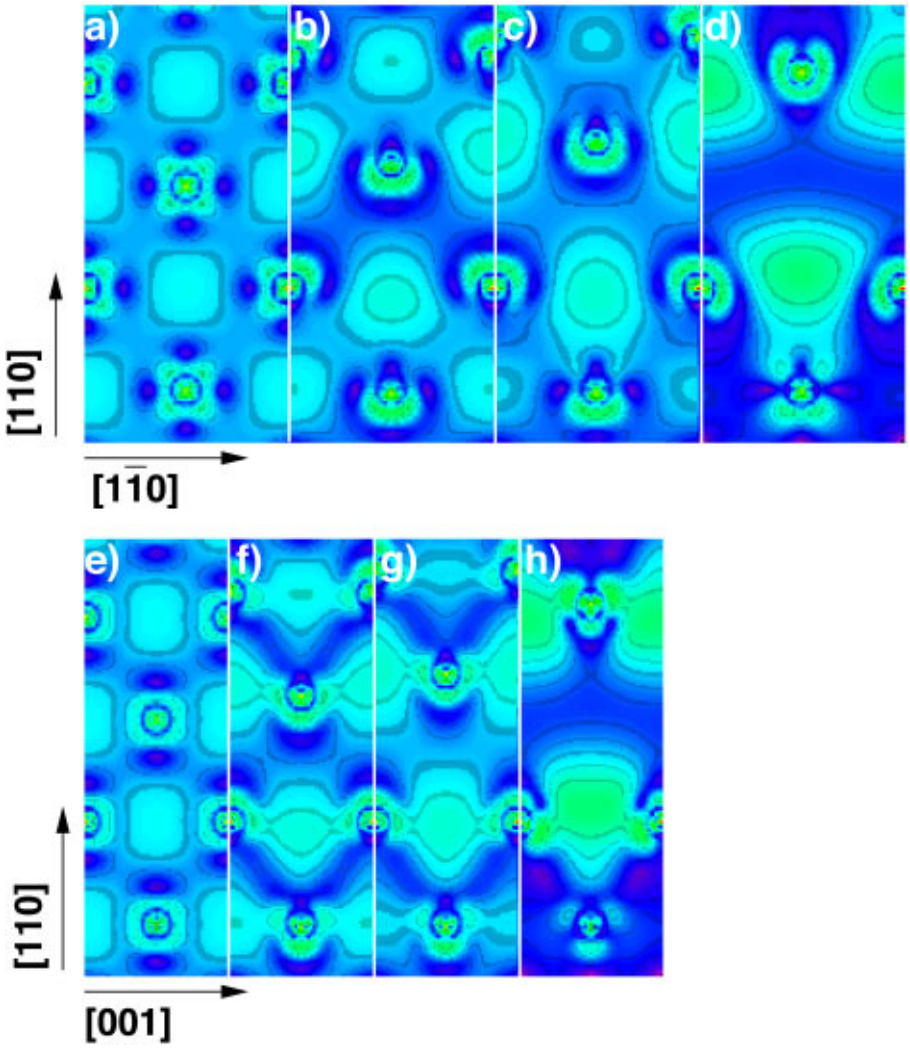

FIG. 10. (Color) Change of the surface state charge density when a W(110) surface is created from a bulk calculation. A single state of the band at $\mathbf{k}=\sqrt{2}\pi/a_0\,(0.35,0.35\sqrt{2},0.35)$ with energy $\epsilon_{\mathbf{k}\nu}=E_F-1.2$ eV is displayed. (a)–(d) in the $[1\bar{1}0]$ direction: (a) bulk, (b) $+0.5$ Å, (c) $+1.0$ Å, and (d) $+2.5$ Å. (e)–(h) in the [001] direction: (e) bulk, (f) $+0.5$ Å, (g) $+1.0$ Å, and (h) $+2.5$ Å.

direction is missing. There is a band in the monolayer band structure with a behavior near the $\bar{S}$ point (at $+0.5$ eV, see Fig. 11) similar to the surface-state band of the W(110) surface but the calculation of the second star coefficient displays no sign reversal (not shown here).

We have thus analyzed that the surface-state band, which leads to anticorrugation in STM images, originates from a hybridization of surface and subsurface states. This concludes the analysis of the electronic structure with respect to the phenomena of image reversal.

E. Comments on Nb(110), Mo(110), Ta(110)

It is well-known[31] that the overall form and structure of the LDOS and of the band structure depend on the crystal symmetry, while the actual peak positions relative to the Fermi energy, peak heights or energy dispersions depend on the crystal potential or chemical element, respectively. Thus, we speculate that the image reversal, predicted for W(110), is a rather general phenomenon for all bcc (110) transition-metal surfaces although the image change may occur at different voltages depending on the metal. Therefore, we have calculated Ta(110) as an additional example of unmagnetic bcc (110) transition-metal surfaces. The corrugation amplitude at a distance of $z_0=4.6$ Å is displayed in Fig. 12. As for W(110) there is a corrugation reversal which in this case occurs at $V=+1.3$ V. Thus in a wide voltage regime around 0 V only anticorrugation images will be observed. Also the change from one corrugation type to the other takes place on a much smaller voltage scale (i.e., the curve is much steeper near the critical voltage). The surface-state band responsible for the effect has its band minimum at an energy of 0.6 eV below E_F. It has shifted up by 0.7 eV compared to W, which is due to the fact that Ta has one electron less. Mo, as another possible candidate, is isoelectronic to W and hence we expect for the Mo(110) surface an image reversal around E_F. Nb is isoelectronic to Ta and we estimate that the bottom of the surface-state band should be also around 0.6 eV below E_F and an image reversal should occur around $V=+1.3$ V.

F. Comments on ferromagnetic Fe(110)

A more complicated scenario may develop for the (110) surfaces of the magnetic bcc $3d$ transition metals Cr, Mn,

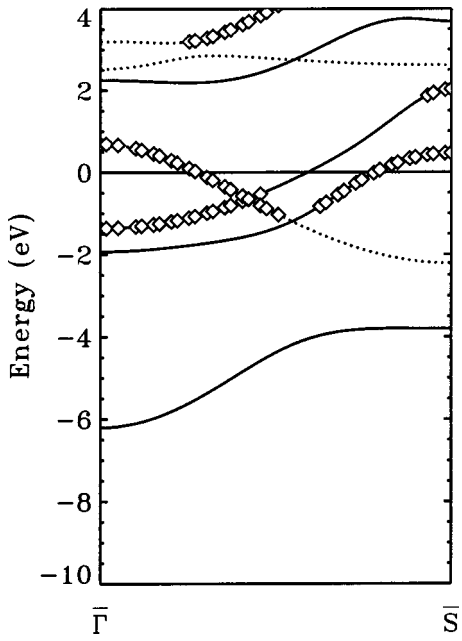

FIG. 11. Calculated surface band structure of a free monolayer of W(110) along the $\overline{\Gamma S}$ direction of the Brillouin zone. States marked with a diamond are localized with more than 20% in the vacuum. The Fermi energy E_F defines the energy zero.

and Fe. The electronic structure is spin-split by an exchange splitting, whose size is proportional to the local magnetic moment. Therefore, the image reversal should occur twice, once for the majority states and once for the minority states. If the majority states are located below E_F and the minority states are located above E_F or a magnetic tip is used, then the observation of both anticorrugations should become possible. In general, however, nonmagnetic tips are used and electrons of one spin character dominate the tunneling current. In this case one expects only the anticorrugation of the leading vacuum spin character. The minor vacuum spin character, which is not necessarily identical to the minority states, may contribute to a small intensity variation of the tunneling current.

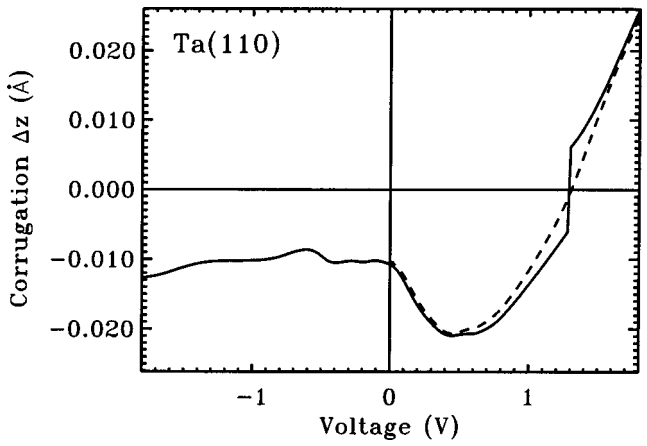

FIG. 12. Dependence of the corrugation amplitude Δz of the Ta(110) surface on the bias voltage. The full line displays $\Delta z = z_{max} - z_{min}$, calculated by Eq. (21), between the lateral points $\mathbf{r}_\parallel$ of maximum and minimum corrugation within the surface unit cell. The dashed line displays $\Delta z = z_{atom} - z_{hollow}$, the corrugation measured between the position of the atom and the hollow site. The distance from the surface was $z_0 = 4.6$ Å.

To explore this further we have investigated ferromagnetic Fe(110) as a typical example of a magnetic bcc transition metal in more detail. Fe has two valence electrons more than W. Since ferromagnetic Fe has a moment of about 2 μ_B, both additional electrons occupy majority states and the number of Fe minority electrons and of W valence electrons per spin state are about the same. Therefore, similar to W, Fe minority spin states should drive the anticorrugation effect at energies close to the Fermi energy, e.g., small bias voltage, and thus should be accessible by STM experiments. The anticorrugation effect driven by the majority electrons may be well below E_F and probably not accessible by STM experiments. We have calculated the electronic structure of ferromagnetic Fe(110). The bulk magnetic moment was determined to $2.06\mu_B$ in good agreement with the experimental value of $2.12\mu_B$. The surface magnetic moment was enhanced to $2.35\mu_B$. As expected we found a spin-split electronic structure. Looking at the LDOS of a surface Fe atom displayed in Fig. 13 we find an exchange splitting of about 2 eV for a surface atom. The minority spin states are the dominating spin character in the vicinity of the Fermi energy. Moreover, at E_F the majority states are mostly bulk states and the minority states are mostly surface states located in the typical bcc bonding-antibonding gap dominating the tunneling current through the vacuum barrier (cf. Fig. 13). Figure 14 exhibits the surface band structures of the Fe(110) minority and majority states along $\overline{\Gamma S}$ direction. Both are similar to the band structure of the W(110) surface (cf. Fig. 6). In particular the surface-state band, responsible for the anticorrugated images of the W(110) surface, can be found for both spin characters. For the Fe minority state, the bottom of the surface-state band is located at about -0.7 eV,[32] indeed close to the value of -1.3 eV for W(110). For majority states, the bottom of the surface-state band is located at -2.4 eV.[32] The zero curvature at the bottom of the surface-state bands lead to narrow peaks in the LDOS of the surface Fe atom and the vacuum exhibited in Fig. 13. Corresponding to the minority-state surface-band starting at -0.7 eV we determined the corrugation-reversal from the anti-corrugated image to the normal STM-image in the minority-state-channel at a voltage of about $+0.7$ V, shown in Fig. 15. Since in general the STM tip is not sensitive to the spin direction of tunneling electrons, majority spin states will also contribute to an image taken at this energy. From Fig. 15 we see, that for this energy range, majority electrons always lead to a normal corrugation pattern and work against the corrugation reversal caused by the minority surface state. However, their contribution to the tunneling current is much smaller than that of the minority states and the image-reversal will take place. The critical voltage at which the reversal takes place is shifted to $+0.4$ V. Since the contributions of majority and minority states to the corrugation amplitude are of different sign the total amplitude becomes extremely small [compare to W(110), Fig. 2]. Thus one might not be able to gain atomic resolution on the Fe(110) surface at all.

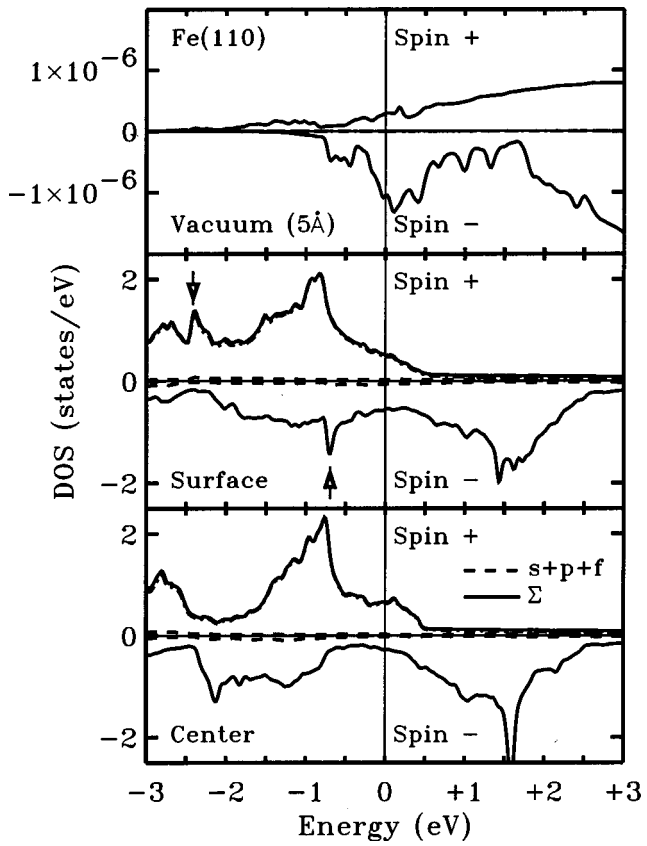

FIG. 13. Spin-resolved density of states of ferromagnetic Fe(110) as a function of energy. Upper part of each panel displays majority states (spin, +), lower part minority states (spin, −). Top panel contains the DOS in the vacuum at a tip sample distance of $z_0=5$ Å in a volume determined by $\delta z_0=1.3$ Å. Middle and bottom panel show the angular momentum decomposed density of states projected in muffin-tin spheres for surface atom and center atom, respectively. The latter corresponds to the bulk LDOS. Full line represents the total contribution while the broken line represents the insignificant amount of $s+p+f$ contribution. Arrows indicate the minimum of the surface state band. The Fermi energy is the origin of energy zero.

VI. SUMMARY

We have presented a detailed theoretical study of STM images for the W(110) surface on the basis of the Tersoff-Hamann model.[2] We compared our calculated STM image with an experimental one and found a good qualitative agreement. Concerning the corrugation amplitude we applied Chen's derivative rule[19] and could explain the enhanced experimental value as compared to the calculated one, calculated on the basis of the Tersoff-Hamann model, by assuming a possible d_{z^2} orbital for the STM tip. Depending on the energy regime, i.e., the applied bias voltage V, we found either a normal image of atomic sites (in case of $V>-0.4$ V) or a reversed image which corresponds to observing the interstices as atoms ($V<-0.4$ V). This is a consequence of the electronic structure of the surface. In the voltage regime, where the image reversal takes place, the corrugation amplitude becomes extremely small, atomic resolution is lost and a stripelike topography may appear. This is consistent with the experimental difficulties finding atomic resolution at negative voltages. By detailed analysis we have shown that a

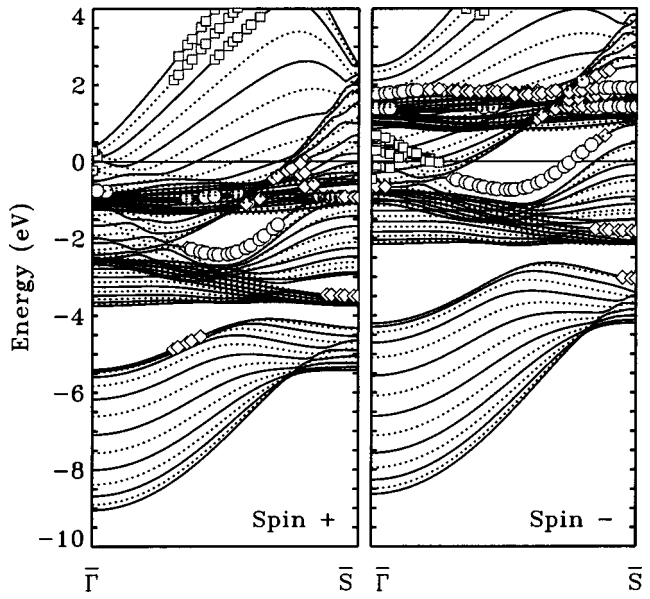

FIG. 14. Calculated surface band structure of Fe(110) majority (left) and minority (right) states along the $\overline{\Gamma S}$ direction of the 2D BZ. States marked with a square, dot, or diamond are localized with more than 5% in the vacuum, more than 60% within the vacuum plus the muffin-tin sphere of the surface atom, or more than 70% within the vacuum plus the muffin-tin spheres of the surface and subsurface atoms, respectively. The Fermi energy E_F defines the energy zero.

competition between a surface state with anticorrugating and a resonance with corrugating charge density is the reason for this unexpected behavior. Since these competing states have different decay lengths into the vacuum, the critical voltage for the image reversal depends also on the tip-surface separation. It increases linearly from -0.4 V at $z_0=4.6$ Å to 0 V at $z_0=7.2$ Å. In the case of Ta(110) anticorrugated STM

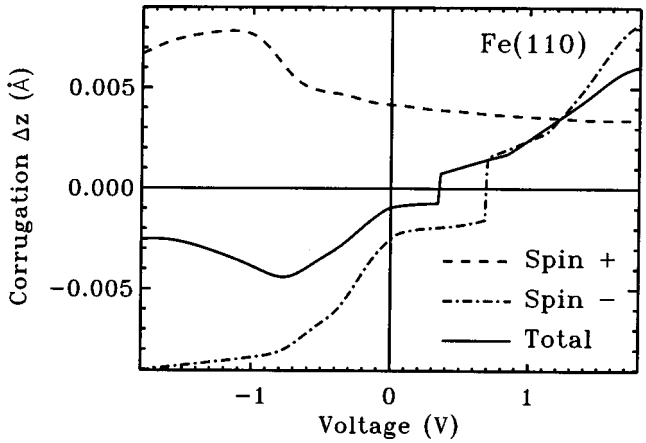

FIG. 15. Dependence of the corrugation amplitude on the bias voltage of the ferromagnetic Fe(110) surface. The full line displays $\Delta z=z_{max}-z_{min}$, calculated by Eq. (21), between the lateral points $\mathbf{r}_\parallel$ of maximum and minimum corrugation within the unit cell at a distance of $z_0=4.5$ Å. The sign of corrugation amplitude has been defined by the sign of the (integrated) second star coefficient. The dashed and dotted-dashed lines display the contributions of majority and minority electrons, respectively. Notice that the total corrugation amplitude is not simply the sum of majority and minority contributions.

images are expected practically over the entire voltage regime available by the STM. The critical voltage at which anticorrugated images change to corrugated ones was shifted to a value of $+1.3$ V and the change takes place in a smaller voltage interval than for W. For Fe(110) the bandstructure is very similar to the ones of W(110) or Ta(110). In the ferromagnetic ground state, the spin splitting of the bands shifts the majority surface state to energies too far below the Fermi energy to be accessible experimentally by STM. However, the image reversal should still be observable for minority spin electrons and should occur at a bias voltage of about $+0.4$ V when both spin directions contribute to tunneling current as for a standard STM. In the not so far future, when spin-polarized STM becomes available, we may observe the different corrugating nature of majority and minority states. In case of a spin-polarized STM the image reversal is expected for 0.7 eV and below 0.7 eV minority states should appear anticorrugated and majority states corrugated.

Since the effect depends only on the electronic structure it seems very likely to be a general phenomena for all transition-metal bcc (110) surfaces although the image change may occur at different voltages depending on the metal under investigation. Experimentally the effect could be identified by scanning a surface with adsorbates of known adsorption site acting as reference in order to distinguish between the two different corrugation patterns of the surface as done for N/Cr(100) by Varga *et al.*[33]

Note added in proof. We recently became aware that the distance dependent $\mathbf{k}_{\|}$ and $\mathbf{G}_{\perp}^{s}$ selection [similar to Eq. (14)] has been used before by Harris and Liebsch [J. Harris and A. Liebsch, Phys. Rev. Lett. **49**, 341 (1982)] to analyze helium scattering at metal surfaces.

ACKNOWLEDGMENTS

Work was supported by the Deutsche Forschungsgemeinschaft under Grant Nos. BL444/1-1 and WI1277/6-1. Computations were performed under the supercomputer grant ''Magnetism, structure and electronic structure of ultrathin films.''

*Electronic address: s.bluegel@fz-juelich.de

[1] G. Binnig, H. Rohrer, Ch. Gerber, and E. Weibel, Phys. Rev. Lett. **49**, 57 (1982); **50,** 120 (1983).
[2] J. Tersoff and D. R. Hamann, Phys. Rev. Lett. **50**, 1998 (1983).
[3] J. Tersoff and D. R. Hamann, Phys. Rev. B **31**, 805 (1985).
[4] R. M. Feenstra, J. A. Stroscio, J. Tersoff, and A. P. Fein, Phys. Rev. Lett. **58**, 1192 (1987).
[5] R. M. Feenstra, J. A. Stroscio, and A. P. Fein, Surf. Sci. **181**, 295 (1987).
[6] J. Dabrowski, H.-J. Müssig, and G. Wolff, Phys. Rev. Lett. **73**, 1660 (1994).
[7] R. B. Capaz, K. Cho, and J. D. Joannopoulos, Phys. Rev. Lett. **75**, 1811 (1995).
[8] Ph. Ebert, B. Engels, P. Richard, K. Schroeder, S. Blügel, C. Domke, M. Heinrich, and K. Urban, Phys. Rev. Lett. **77**, 2997 (1996).
[9] B. Voigtländer, V. Scheuch, H. P. Bonzel, S. Heinze, and S. Blügel, Phys. Rev. B **55**, R13 444 (1997).
[10] J. A. Stroscio, D. T. Pierce, A. Davies, R. J. Celotta, and M. Weinert, Phys. Rev. Lett. **75**, 2960 (1995).
[11] A. Biedermann, O. Genser, W. Hebenstreit, M. Schmid, J. Redinger, R. Podloucky, and P. Varga, Phys. Rev. Lett. **76**, 4179 (1996).
[12] M. C. Desjonqueres and D. Spanjaard, *Concepts in Surface Physics* (Springer-Verlag, Heidelberg, 1996).
[13] V. M. Hallmark, S. Chiang, J. F. Rabolt, J. D. Swalen, and R. J. Wilson, Phys. Rev. Lett. **59**, 2879 (1987).
[14] J. Wintterlin, J. Wiechers, J. Brune, T. Gritsch, H. Höfer, and R. J. Behm, Phys. Rev. Lett. **62**, 59 (1989).
[15] Ch. Wöll, S. Chiang, R. J. Wilson, and P. H. Lippel, Phys. Rev. B **39**, 7988 (1989).
[16] G. Doyen, D. Drakova, and M. Scheffler, Phys. Rev. B **47**, 9778 (1993).
[17] In this paper the vertical distance (z) is always measured between the center of the surface and tip atom (nucleus-nucleus distance).
[18] J. Bardeen, Phys. Rev. Lett. **6**, 57 (1961).
[19] C. J. Chen, J. Vac. Sci. Technol. A **6**, 391 (1988); Phys. Rev. B **42**, 8841 (1990); Phys. Rev. Lett. **65**, 448 (1990); C. J. Chen, *Introduction to Scanning Tunneling Microscopy* (Oxford University Press, Oxford, 1993).
[20] E. Wimmer, H. Krakauer, M. Weinert, and A. J. Freeman, Phys. Rev. B **24**, 864 (1981); M. Weinert, E. Wimmer, and A. J. Freeman, *ibid*. **26**, 4571 (1982).
[21] Four-points Lagrange formulas for equally spaced abscissas are used to compute the first and second derivative; see, e.g., *Handbook of Mathematical Functions*, edited by M. Abramowitz and I. A. Stegun (Dover, New York, 1972).
[22] W. Sacks, S. Gauthier, S. Rousset, J. Klein, and M. A. Esrick, Phys. Rev. B **36**, 961 (1987).
[23] P. Hohenberg and W. Kohn, Phys. Rev. B **136**, 864 (1964).
[24] U. von Barth and L. Hedin, J. Phys. C **5**, 1629 (1972).
[25] V. L. Moruzzi, J. F. Janak, and A. R. Williams, *Calculated Electronic Properties of Metals* (Pergamon, New York, 1978).
[26] R. J. Smith, C. Hennessy, M. W. Kim, C. N. Whang, M. Worthington, and X. Mingde, Phys. Rev. Lett. **58**, 702 (1987).
[27] S. L. Cunningham, Phys. Rev. B **10**, 4988 (1974).
[28] M. Bode, R. Pascal, and R. Wiesendanger, Surf. Sci. **344**, 185 (1995).
[29] S. Ohnishi and M. Tsukada, Solid State Commun. **71**, 391 (1989).
[30] R. H. Gaylord, K. H. Jeong, and S. D. Kevan, Phys. Rev. Lett. **62**, 2036 (1989); E. Rotenberg and S. D. Kevan, *ibid*. **80**, 2905 (1998).
[31] For a comparison of bandstructures and LDOS of different fcc and bcc transition metals see, for example, Ref. 25.
[32] We determined the minimum of the surface-state band for ferromagnetic bcc Fe(110) calculated at the experimental lattice constant of $a_0 = 5.43$ a.u. at -0.45 eV and -2.35 eV for the minority and majority states, respectively.
[33] M. Sporn, E. Platzgummer, M. Pinczolits, W. Hebenstreit, M. Schmid, W. Hofer, and P. Varga, Surf. Sci. **396**, 78 (1998).